Impurity-density calculations from spectroscopic measurements of visible and uv line emission on the Alcator-*C* tokamak

J. C. Moreno and E. S. Marmar
Plasma Fusion Center, Massachusetts Institute of Technology, Cambridge, Massachusetts 02139
(Received 25 May 1984; revised manuscript received 19 February 1985)

Densities of C, O, and Si impurities during the steady-state portion of Alcator-*C* discharges have been computed from spectroscopic measurements of the absolute brightnesses of visible and uv emission lines in combination with a one-dimensional transport calculation which models the charge-state and emissivity profiles. Profiles of all the charge states of a particular impurity were calculated by utilizing independent measurements of plasma density and temperature and by solving the coupled system of transport and rate equations connecting the ionization states. These profiles were then used to calculate emissivity profiles by solving the matrix equation relating the level populations through collisional excitation, collisional deexcitation, spontaneous emission, inner-shell ionization, and cascades from upper levels. Three different types of limiters (molybdenum, graphite, and SiC-coated graphite) have been used on the Alcator-*C*. It was observed that the principal impurities in the plasma, under most conditions, were determined by the type of limiter material being used. However, the source of the impurities could be either the wall or the limiters, since it has been shown that the wall becomes coated with limiter material. A significant influx of impurities directly from the limiters was often seen during the application of lower-hybrid-frequency rf power to the plasma.

I. INTRODUCTION

The density and spatial distribution of impurities in a tokamak discharge can greatly influence the characteristics of the plasma. Even a modest amount of impurities can affect energy confinement, especially the heavier impurities which do not become fully stripped and radiate mostly from the central region of the plasma. Too large a concentration of impurities can cause disruptions or result in considerable radiative power loss.[1] For these reasons it is essential that plasmas in reactor relevant regimes be kept clean ($Z_{\rm eff}\sim 1$). However, small amounts of light impurities can be tolerated, and may in fact be beneficial, since they radiate from the edge region of the plasma and should therefore help keep the temperature at the edge low. This, in turn, can reduce sputtering from edge structures.[2] Spectroscopic instruments, operating from the visible to the x-ray region of the spectrum, are typically used to study impurities in tokamak plasmas.[3–5] The principal instrument used in this experiment is a spectrograph covering the visible and uv portion of the spectrum (2000–8000 Å). Additionally, some of the data presented are from measurements taken using vacuum uv monochromators.

In Sec. II, the spectrograph and the Alcator-*C* tokamak will be described in more detail. A brief survey will also be given of diagnostics that routinely operate on the Alcator tokamak. Section III contains an explanation of the theoretical model and numerical computations which were used to obtain absolute impurity densities. Section IV shows typical examples of emissivity, brightness, and impurity-density profiles, calculated from the numerical simulations. Finally, Sec. V contains a study of how impurity emission from Alcator-*C* depends on the type of limiter material being used. A comparison is shown of low- to medium-*Z* impurities resulting from molybdenum, graphite, and SiC-coated graphite limiters. The influx of impurities into the plasma during lower-hybrid-frequency rf heating is also examined.

II. EXPERIMENTAL ARRANGEMENT

Most of the measurements reported here have been obtained using a 1.5 m grating spectrograph with a Wadsworth mounting. The instrument has a reciprocal linear dispersion of nominally 10.8 Å/mm in first order using a concave holographic grating with 600 G/mm. One of the advantages of this instrument's wavelength range is that no vacuum is needed and the absolute calibration, using a tungsten lamp, is straightforward and relatively accurate. The disadvantage is that it is more difficult, theoretically, to obtain impurity densities from the characteristic lines in this part of the spectrum, because the emission is mostly from the edge region of the plasma where there is more turbulence and the plasma parameters are less well known. In addition, as will be discussed later, poloidal and toroidal asymmetries are generally important. There are two modes of operation for this spectrograph. The first consists of using a film attachment that can take film spectra in the range 2000–8000 Å. Film spectra were recorded every few months in order to obtain a survey of the emission lines and verify which impurities were present in the plasma. A portion of a densitometer trace of one such spectrum is shown in Fig. 1. In the usual mode of operation, the absolute brightnesses of emission lines were measured as a function of time. Up to ten

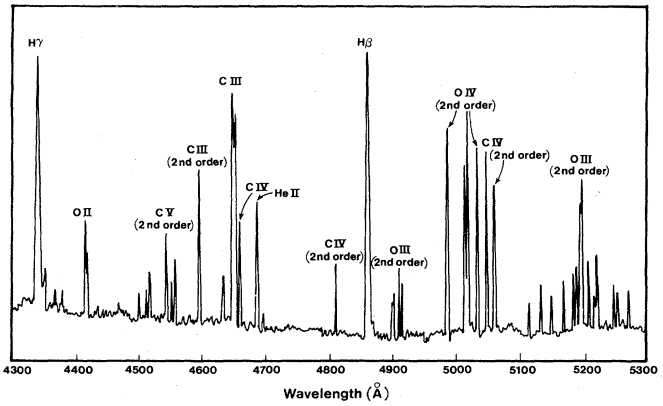

FIG. 1. Densitometer trace of a film spectrum, integrated over several plasma shots.

emission lines were recorded simultaneously by sending the light through quartz optical fibers to photomultiplier (PM) tubes as shown in Fig. 2. The fiber arrays are connected at one end to a brass plate which attaches along the exit plane of the spectrograph. Slots had been milled into the plate at the locations where chosen emission lines were focused on the exit plane. The fibers transfer the light passing through the slots to the photomultiplier tubes, whose output signals are then digitized and stored on a computer.

Measurements from other diagnostics were used to supplement the spectrograph data. Two vacuum uv monochromators were utilized: one is a grazing incidence monochromator covering the wavelength range 50—500 Å; the other is a normal incidence monochromator covering the range 1200—2300 Å. Electron density is measured on Alcator-*C* using a five-chord laser interferometer.[6] Electron temperatures are measured by Thomson scattering, ECE emission,[7] and soft x-ray emission.[8]

The Alcator-*C* tokamak is a high-field, high-density plasma confinement device which has a major radius of 64 cm and a minor radius of 16.5 cm. A typical discharge for which these data were taken had the following conditions: toroidal field $B_T=80$ kG; line-average electron density $\bar{N}_e=2\times10^{14}$ cm^{-3}; central electron temperature $T_e=1500$ eV; and plasma current $I_p=450$ kA. The range of plasma parameters is $B_T=40$—120 kG, $\bar{N}_e=1\times10^{13}$—1×10^{15} cm^{-3}, and $T_e=1$—3 keV.

Characteristic time histories of impurity lines are shown in Fig. 3. They consist of an ionization spike at the beginning of the discharge when the plasma is rapidly being heated and then, after about 10 msec, the ionization states reach a steady-state equilibrium.[9] It was during this steady-state portion of the discharge that the impurity densities were calculated.

Impurity concentrations were computed for only a limited range of plasma densities, 1×10^{14} cm$^{-3}<\bar{N}_e<2\times10^{14}$ cm^{-3}, where the plasma was well behaved and its parameters could be accurately measured. An example of the variation of C III and C V brightnesses with line-average electron density can be seen in Fig. 4. For $\bar{N}_e<1\times10^{14}$ cm^{-3}, the plasma exhibits nonthermal effects and the dominant contribution to Z_{eff} is from heavier impurities (with molybdenum limiters), while for $\bar{N}_e>2\times10^{14}$ cm^{-3} the plasma experiences what are referred to as "marfes." A marfe is believed to be a thermal instability which results in a poloidally asymmetric high-density region of plasma near the limiter radius and usually close to the inside major radius edge of the plasma.[10]

III. NUMERICAL MODELING: THEORY

The method used here to obtain impurity densities begins with the determination of the theoretical charge-state profiles based upon the measured electron density and temperature profiles and an impurity transport model. A good review of different transport models can be found in Ref. 11. Charge-state profiles as a function of time are computed first by solving the coupled system of transport and rate equations[12,13] connecting the ionization states:

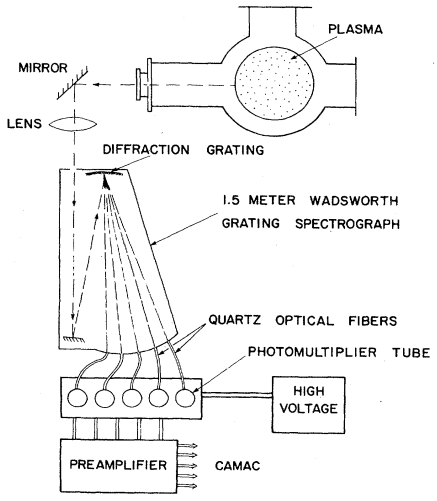

FIG. 2. Experimental setup of the visible uv spectrograph (2000—8000 Å).

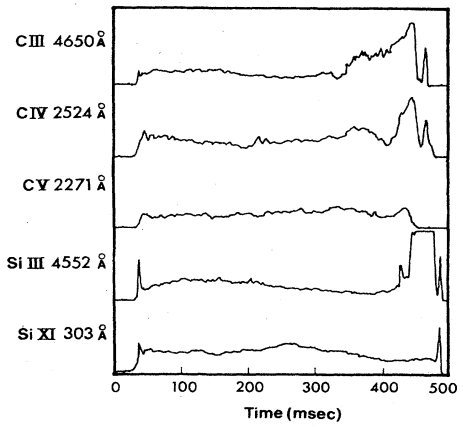

FIG. 3. Time evolution of C III, C IV, C V, Si III, and Si XI line emissions for an ohmic discharge. $I_p=450$ kA, $N_e=2.5\times10^{14}$ cm^{-3}, and $B_T=80$ kG.

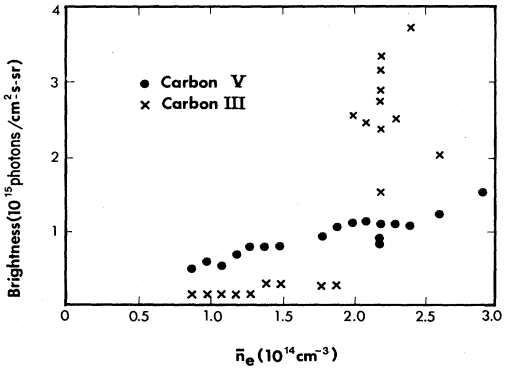

FIG. 4. C III and C V plotted as a function of line-average electron density with all other plasma parameters remaining constant. $I_p=400$ kA and $B_T=100$ kG. For line-average electron densities above 2×10^{14} cm^{-3} the effect of "marfes" can be seen in the C III emission.

$$\frac{\partial N^1(r,t)}{\partial t}=-N_eN^1I(1,2)+N_eN^2R(2,1)-\nabla\cdot\Gamma^1\ ,$$

$$\frac{\partial N^2(r,t)}{\partial t}=N_eN^1I(1,2)-N_eN^2I(2,3)+N_eN^3R(3,2)-N_eN^2R(2,1)-\nabla\cdot\Gamma^2\ ,$$

$$\ldots\ ,$$

$$\frac{\partial N^z(r,t)}{\partial t}=N_eN^{z-1}I(z-1,z)-N_eN^zR(z,z-1)-\nabla\cdot\Gamma^z\ ; \tag{1}$$

$$\Gamma^i(r)=-D\nabla N^i-N^iv\ ,$$

$$v(r)=v_ar/r_L\ ,$$

$$D(r)=\text{const}\ ,$$

where N^i is the density of the ith ionization state, $N^1(r,0)$ is the initial density of the singly ionized impurity, Γ^i is the flux, $I(i,j)$ is the ionization rate[14] from charge state i to state j, $R(i,j)$ is the recombination rate,[15] D is the diffusion coefficient, $v(r)$ is the convection velocity, v_a is a constant, r_L is the minor radius, and z is the nuclear charge. Impurity-injection experiments performed on Alcator-A and -C (Ref. 16) showed that impurity transport was inconsistent with neoclassical theory and instead could be described solely by an anomalous diffusion term or by diffusion plus a small amount of convection. Empirical relationships for the confinement time τ and the diffusion coefficient D, as a function of various plasma parameters, were determined. These formulas for τ and D, which assumed no inward convection, were initially used in the computation. To investigate the effects of convection, an analytical expression for the confinement time is employed,[17]

$$\tau=\frac{77+S^2}{56+S^2}\frac{e^s-S-1}{4S^2}\frac{r_L^2}{D}\ \text{sec}\ , \tag{2}$$

where S is the dimensionless "convection parameter" given by $S=r_Lv_a/2D$. Effects of convection can be included by choosing an appropriate value for v_a and adjusting D so that the confinement time given by Eq. (2) remains the same.

Finding a steady-state solution of Eq. (1) requires integrating the equations for several confinement times until essentially all the particles are lost. The time integral density profiles are solutions for a steady-state source as explained in the Appendix.

Once the charge-state profiles have been computed, the next step in the calculation of the absolute charge-state density is to compute the emissivity and brightness profiles and then finally to normalize all the profiles to the measured central-chord brightness of an emission line. The intensity of the emission lines observed here are determined mainly by electron impact excitation and spontaneous decay between the separate energy levels of the ion. Rate coefficients[18–23] for each of the individual transitions, from quantum number $n=1$ to $n=3$ or 4, are used in the calculations. The excitation rate coefficients were determined by fitting a function to the collision strengths of each transition. This function of electron energy, $f(E)$, is then integrated over all energies, using a Maxwellian distribution, to get the excitation rate coefficient as a function of electron temperature. Higher n levels have been included by using expressions for average spontaneous decay rates and average excitation rates. The emissivity of a photon is directly related to the density of the excited state from which the line was emitted, through the relation $E(p,q)=N^z(p)A(p,q)$, where $A(p,q)$ is the spontaneous decay rate[24,25] from level p to q and $N^z(p)$ is the density of level p in charge state z. Using the density of this excited state and assuming a steady state, a matrix representing a system of m equations is solved to determine the density of all the individual energy levels up to $n=4$ and the average density for $n>4$. The equations are the following:

$$\frac{\partial N^z(2;r)}{\partial t}=0=\sum_pN^z(p)A(p,2)-N^z(2)A(2,1)+N_e\sum_pN^z(p)X(p,2)-N_eN^z(2)\sum_pX(2,p)+N_eN^{z-1}I_c(z-1,z;2)\ ,$$

$$\frac{\partial N^z(3;r)}{\partial t}=0=\sum_pN^z(p)A(p,3)-N^z(3)\sum_pA(3,p)+N_e\sum_pN^z(p)X(p,3)-N_eN^z(3)\sum_pX(3,p)+N_eN^{z-1}I_c(z-1,z;3)\ , \tag{3}$$

$$\ldots\ ,$$

$$\frac{\partial N^z(m+1;r)}{\partial t}=0=-N^z(m+1)\sum_pA(m+1,p)+N_e\sum_pN^z(p)X(p,m+1)\ ,$$

where $X(p,q)$ is the collisional excitation (or deexcitation) rate from level p to q and I_c is the collisional inner-shell ionization rate. Note that it is not necessary to include the equation for the ground-state density since the density of one of the excited states is computed directly from the measured brightness of an emission line and we are left with m equations and m unknowns.

Level populations (for $n<4$) are determined principally by spontaneous decay and electron impact excitation among low n energy levels. However, collisional inner-shell ionization and cascading from high-n levels also influence, to a lesser degree, the level populations and have therefore been included in the calculations. Dielectronic recombination and charge exchange have been neglected here. These processes could be important in determining the population of high-n energy levels but will have negligible effect on the intensities of the measured lines.

Collisional inner-shell ionization is an atomic process where ionization occurs through the loss of an inner-shell electron, leaving the ion in an excited state. This rate is much less than the total ionization rate and therefore has no effect on the charge-state distribution. However, it can slightly change the population of excited energy levels and has therefore been included in Eq. (3).

Excited states with high quantum numbers ($n>4$) can influence the population of low n states through cascades. This effect has been taken into account by using average transition rates between quantum levels n_i and n_j.[26,27] Including these higher-n excited levels changes the computed density of ionization states, particularly those with metastable levels (e.g., C III, O V). This is due to the fact that these ions with metastable states have a relatively large population in the high-n energy levels and therefore cascades can appreciably populate the low-energy levels.

Equation (3) was represented by a matrix and solved every 0.1 cm along the minor radius with the input initially being a radially constant emissivity profile of the measured emission line. The solution at each radial location yielded the densities of the energy levels, which were then added together to give the total charge-state density. This charge-state density was made to agree with the steady-state charge-state profile by adjusting the emissivity profile. Then by repeating this procedure iteratively it was possible to obtain an emissivity profile which was self-consistent with the charge-state profile and also normalized to the measured central chord brightness. Computed emissivity and brightness profiles for C III and C V are shown in Fig. 5. From this same procedure, the absolute density of energy levels in each charge state was computed as a function of radius. Figure 6 shows the level populations for the first few excited states of C III at a chosen radius. As can be seen the triplet state $2s\,2p\ ^3P$, which is metastable, has a larger population than the ground state. The brightness of all the emission lines included in the code were also computed and compared to measured brightnesses of lines which could be observed. The agreement was in general within a factor of 2.

IV. NUMERICAL MODELING: RESULTS

The numerical model and the absolute brightness of emission lines were used to determine densities of impurities for a wide range of plasma conditions and with three types of limiters: molybdenum, graphite, and SiC-coated graphite. For plasma densities above $N_e=1\times10^{14}$ cm^{-3}, the dominant impurities in ohmically heated Alcator-C discharges were found to be carbon, oxygen, and silicon, depending on the limiter being used. The main emission lines used to calculate densities were C III (4650 Å), C IV (1550 Å), C V (2271 Å), O V (2781 Å), Si III (4552 Å), and Si XI (303 Å). Measured brightnesses of the lines were reproducible from shot to shot if the plasma density and current were kept constant and no major disruptions occurred. Variations in plasma conditions, and the application of lower-hybrid rf power,[28] were found to influence significantly the impurity level in the plasma. The impurity calculation described in the previous section requires independent measurements of electron temperature and density profiles (Fig. 7). The electron temperature profile has been studied extensively on Alcator-C by measuring second harmonic electron cyclotron emission[7] and under most conditions the profile is well approximated by a Gaussian of width a_T given by

$$a_T=\left[\frac{3}{2}\frac{q_0}{q_L}\right]^{1/2} r_L \text{ cm}, \tag{4}$$

where q_0 is the safety factor on axis and q_L is the safety factor at the limiter radius. The electron density profile as measured by a laser interferometer is roughly described

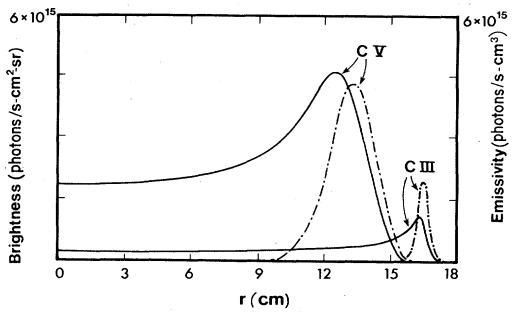

FIG. 5. Computed emissivity and brightness profiles of C III (4650 Å) and C V (2271 Å). The solid lines are brightnesses while the dashed lines are emissivities.

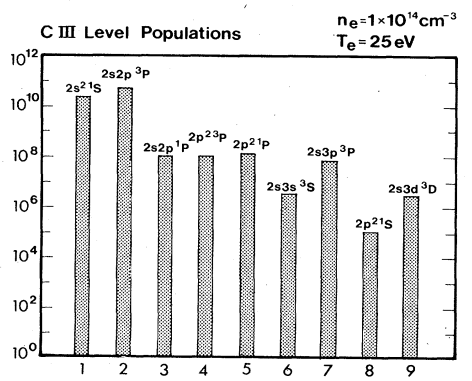

FIG. 6. Densities of lowest energy levels of C III at a specific plasma radius.

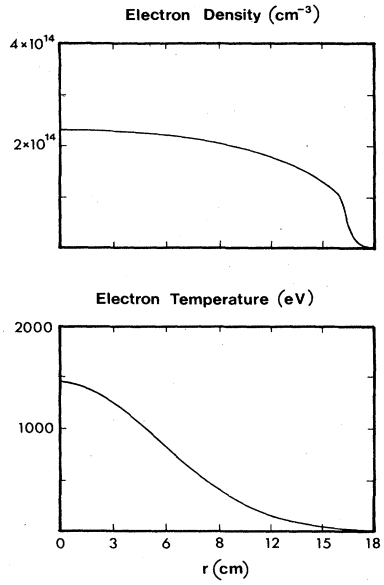

FIG. 7. Typical T_e and N_e profiles used in the impurity calculation.

by a parabolic function, $[1-(r/a)^2]^m$, where m is typically between 0.5 and 1. The temperature and density in the shadow of the limiter, where the lowest charge states exist, have been measured with Langmuir probes,[29] and it was found that T_e is nearly constant in this region while N_e decreases exponentially in radius with a scrape-off length of typically 0.3 cm.

A representative plasma shot (using graphite limiters) is shown in Fig. 8, where the top trace is the plasma current, the second trace is the central chord averaged electron density, the third trace is the central soft x-ray emission (photon energy greater than 1 keV), and the bottom trace is the continuum emission near 5360 Å, due primarily to free-free bremsstrahlung. For these steady-state plasma conditions, Fig. 9 shows the simulated charge-state profiles for carbon calculated with the transport code (assuming $v_a=0$ cm/sec, $D=3400$ cm^2/sec). Including modest inward convection causes the profile of fully ionized low-Z impurities to be more peaked, while partially ionized species are only slightly affected. Figure 10 shows a plot of the total C density for $S=0$, $S=\frac{1}{2}$, and $S=1$. The amount of convection usually chosen is $S\sim\frac{1}{2}$, which yields a flat Z_{eff} profile, consistent with profiles from visible bremsstrahlung measurements.[30]

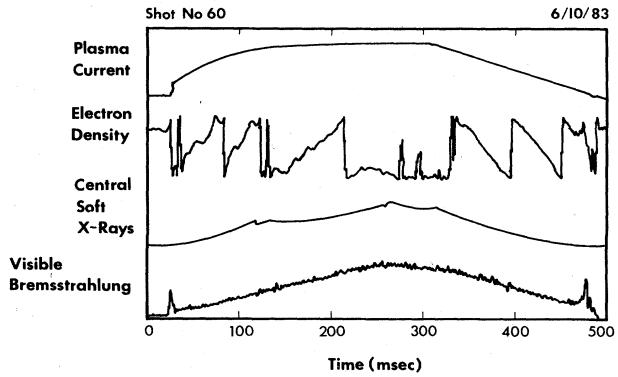

FIG. 8. Typical ohmic discharge. The top trace is the plasma current, the second trace is the line-average electron density (0.55×10^{14} cm^{-3}/fringe), the third trace is the soft x-ray emission, and the bottom trace is the visible continuum emission (5360 Å).

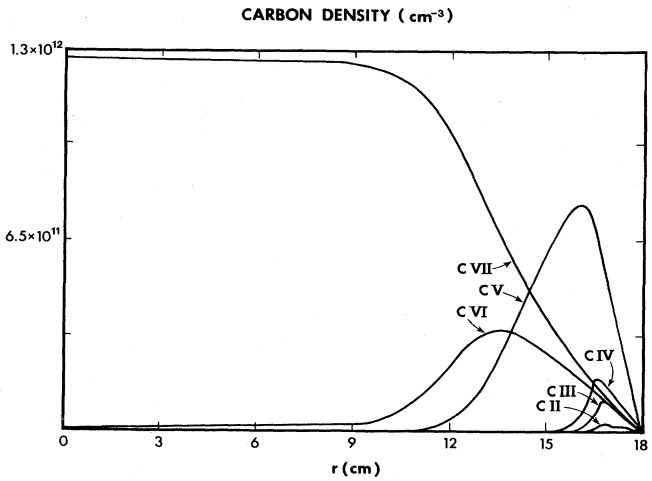

FIG. 9. Computed profiles of all the ionized states of C assuming no inward convection ($S=0$).

An analysis of the various uncertainties in our measurement will now be reviewed. The possible sources of error are listed below.

(a) Calibration, ±20%;
(b) Transport model, ±50%;
(c) T_e and N_e profiles, ±50%;
(d) Atomic rates, ±75%;
(e) Asymmetries, ±50%.

Calibration of the spectrometers was not a significant source of error compared to the other uncertainties. The error in the transport model was due to uncertainty in choosing the correct combination of diffusion and convection in the code. Electron density and temperature profiles could not be measured for every shot which accounts for the relatively large error that is given. The ionization,

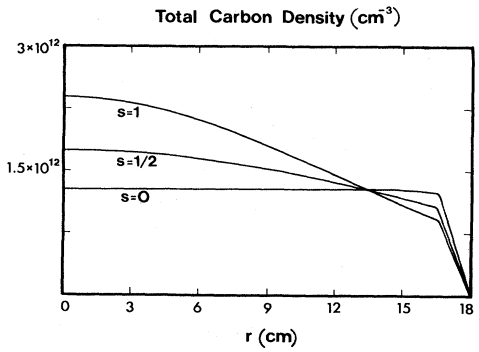

FIG. 10. Total C density evaluated for three different values of the convection parameter S.

recombination, and excitation rates that were used are theoretical values. The error in these rates was estimated by comparing different sources. Finally, poloidal and toroidal asymmetries in lines emission[31–33] could be a source of error for the low charge states. By changing the input values in the numerical simulation by amounts equivalent to the estimated errors listed above, it was determined that the total uncertainty in the computed impurity density was approximately a factor of 2. This was consistent with a comparison of the measured brightnesses of different emission lines of the same impurity. As another check of the accuracy of this method, one can compare our calculated value for Z_{eff} to the value obtained from visible bremsstrahlung measurements. For a plasma where graphite limiters were used, the dominant impurity was carbon and typical values were found to be, $Z_{\text{eff}}(\text{calculated}) = 1.25 \pm 0.15$, as compared to $Z_{\text{eff}}(\text{bremsstrahlung}) = 1.5 \pm 0.2$.

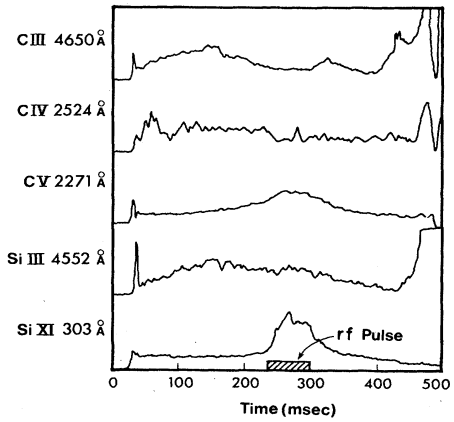

FIG. 11. The rf pulse is applied at about 230 msec and stays on for 70 msec. An increase can be seen in C V and Si XI emission, while no obvious increase is observed in the lower ionization states.

V. LIMITER STUDIES

Experiments were conducted on Alcator-*C* to investigate changes in impurity concentrations during the use of different types of limiters. Table I shows measured central chord brightnesses, computed densities, and Z_{eff} values of C, O, and Si under similar plasma conditions for four periods of time when three different limiter sets were used. All these brightness measurements were made under the same plasma conditions, so although the absolute values for impurity densities may contain some error, the trends that were observed were very reproducible and seen in all lines of each impurity. The limiters that were initially used on Alcator-*C* for several years were made of molybdenum. Spectroscopic measurements made during the use of molybdenum limiters revealed that the O and C density for a typical run were comparable, and lesser amounts of N were also present. When graphite limiters were installed in the device, the C density increased a factor of 4, while the O density immediately decreased a factor of 10, leaving Z_{eff} unchanged. A similar lack of oxygen was observed in the TM-G experiment, where the entire first wall was constructed from graphite.[34] Switching back to molybdenum limiters after several months of operation with graphite limiters resulted in only a slight decrease in C density indicating that the walls were now a significant source of C entering the plasma. A gradual increase of O density occurred over the period of several weeks with the Mo limiters. Next, a SiC-coated graphite limiter was installed on Alcator-*C*. It was found that the dominant impurity was C, whose density was typically a factor of 10 or more larger than Si. Although no quantitative study has been made here of Mo density in Alcator-*C*, it has been observed previously[35] that Mo also becomes deposited on the wall and will remain in the machine even after the Mo limiters are removed. However, Mo only plays a significant role in discharges with $\bar{N}_e < 1 \times 10^{14}$ and while using Mo limiters.

The application of lower-hybrid-frequency rf auxiliary heating to the discharge resulted in increased impurity levels, particularly for rf power > 500 kW, where Z_{eff} increased strongly with power.[28] Figure 11 shows a plasma shot with lower-hybrid radio frequency (LHRF) heating (rf power $= 800$ kW), in which T_e increased by 500 eV. It was observed that, in the course of an rf pulse, the emission from higher ionization states of Si and C increased substantially (depending on plasma density and rf power), while a smaller relative effect was seen for the lower ionization states. This increase in impurity emission cannot be accounted for by the increase in T_e. However, it is

TABLE I. Comparison of impurity densities for different limiters.

$\bar{n}_e = 2 \times 10^{14}$ cm^{-3}
$T_e = 1500$ eV
$I_p = 450$ kA
$B_T = 80$ kG

Limiter	C brightness (photons/sec cm^2 sr)	O brightness (photons/sec cm^2 sr)	C density (cm^{-3})	O density (cm^{-3})	Si density (cm^{-3})	Z_{eff}
Molybdenum	4.8×10^{14}	1.9×10^{14}	4.5×10^{11}	7.1×10^{11}	a	1.23
Graphite	1.8×10^{14}	2.3×10^{13}	1.7×10^{12}	8.7×10^{10}	a	1.24
Molybdenum	1.6×10^{15}	1.6×10^{14}	1.5×10^{12}	5.9×10^{11}	a	1.34
SiC-coated Graphite	1.6×10^{15}	2.1×10^{13}	1.5×10^{12}	7.9×10^{10}	1.8×10^{10}	1.23

[a]Not observed.

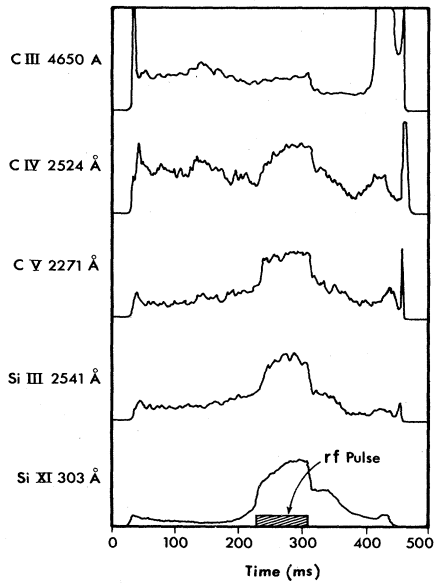

FIG. 12. A significant influx of impurities occurs during the rf pulse. Even the low charge states show an increase in emission during rf, though not as large a relative increase as the higher charge states.

consistent with assuming that the source of Si and C from the wall is at least comparable to the source from the limiters during a normal ohmic discharge, but the limiters become the main source of impurities when LHRF is turned on. The lower charge states show less of a relative increase in brightness during rf than the higher charge states because an impurity coming off the limiter will be partially ionized before it can travel toroidally to where it can be viewed by one of the spectrometers, which were at nonlimiter ports. Limiters were placed 180° apart toroidally, while the ports are located every 60° toroidally. The densities of Si and C during the rf pulse were estimated by the increase in brightness of Si XI and C V lines. This method gave a lower limit to the increase in impurity density because of the substantial toroidal asymmetry of edge impurity emission during rf. An unusually large injection of Si and C, after rf is applied, can be seen in Fig. 12, where even the low charge states show a marked increase in brightness.

VI. CONCLUSIONS

The principal impurities measured in Alcator-*C* plasmas for $\bar{N}_e > 1\times10^{14}$ cm^{-3} were C, O, and Si. Impurity densities were calculated with a numerical simulation consisting of two parts, first, a transport model that computes charge-state profiles and, second, a model determining the level populations of each charge state. These two models were combined, along with absolute brightness measurements of impurity lines, to determine impurity-density profiles of all charge states. Impurity densities showed consistency among brightnesses of lines from different charge states of the same element, and also showed reasonable agreement with independent measurements of Z_{eff}. The walls were a significant source, if not the main source, of low Z impurities during a typical ohmic discharge. An interesting effect was the large decrease in oxygen concentration when Mo limiters were replaced by graphite. Depositing LHRF power into the plasma resulted in a significant influx of impurities from the limiters. The increase of Z_{eff} with lower hybrid heating was particularly strong for LHRF power greater than 500 kW.

ACKNOWLEDGMENTS

We wish to thank J. Terry for useful comments and discussions. The assistance of the rest of the Alcator group is also gratefully acknowledged. This work was supported by the U.S. Department of Energy under Contract No. DE-AC02-78ET51013.

APPENDIX

This appendix shows how the solution to Eq. (1) with a steady-state source is obtained by integrating the solution to the initial source problem over time. Equation (1) can be written in the form

$$\frac{\partial f(x,t)}{\partial t}+\beta f(x,t)=0\ , \tag{A1}$$

where β is a time-independent linear differential operator and $f(x,t)$ is a function with the boundary conditions, $f(x,0)=S_0(x)\tau$ and $f(x,\infty)=0$. $S_0(x)$ is a source function and τ is the time interval for the source. The equation of interest for a steady-state source is

$$\beta h(x)=S_0(x)\ . \tag{A2}$$

The solution we seek is $h(x)$. Integrating Eq. (A1) over time with the limits 0 and ∞ yields

$$\int_0^\infty \frac{\partial f(x,t')}{\partial t'}dt'+\int_0^\infty \beta f(x,t')dt'=0\ . \tag{A3}$$

Since β does not depend on t', it can be taken outside the integral. In addition we can utilize the boundary conditions at $t=0$ and $t=\infty$ to write the equations as

$$\beta\int_0^\infty f(x,t')dt'=S_0(x)\tau\ , \tag{A4}$$

and thus by inspection

$$h(x)=\frac{1}{\tau}\int_0^\infty f(x,t')dt'\ , \tag{A5}$$

This is the steady-state solution of interest.

[1]R. V. Jensen, D. E. Post, W. H. Grasberger, C. B. Tarter, and W. A. Locke, Nucl. Fusion **14**, 289 (1974).
[2]G. M. McCracken and P. E. Stott, Nucl. Fusion **19**, 889 (1979).
[3]Equipe TFR, Nucl. Fusion **18**, 647 (1978).
[4]C. Breton, C. DeMichelis, and M. Mattioli, Tokamak Fontenay-aux-Roses Report No. EUR-CEA-FC-1060, 1980 (unpublished).
[5]C. DeMichelis and M. Mattioli, Nucl. Fusion **21**, 677 (1981).
[6]S. M. Wolfe, K. J. Button, J. Waldman, and D. R. Cohn, Appl. Opt. **15**, 2645 (1976).

[7]S. E. Kissel, Ph.D. thesis, Massachusetts Institute of Technology, 1982, Plasma Fusion Center Report No. PFC/RR-82-15, 1982 (unpublished).
[8]J. E. Rice, private communication.
[9]J. L. Terry, K. I. Chen, H. W. Moos, and E. S. Marmar, Nucl. Fusion **18**, 485 (1978).
[10]B. Lipschultz, B. Labombard, E. Marmar, M. Pickrell, J. Terry, R. Watterson, and S. Wolfe, Nucl. Fusion **24**, 977 (1984).
[11]R. J. Hawryluk. S. Suckewer, and P. Hirshman, Nucl. Fusion **19**, 607 (1979).
[12]S. A. Cohen, J. L. Cecchi, and E. S. Marmar, Phys. Rev. Lett. **35**, 1507 (1975).
[13]E. S. Marmar, Ph.D. thesis, Princeton University (unpublished).
[14]W. Lotz, Astrophys. J., Suppl. Ser. **14**, 207 (1967).
[15]M. Mattioli, Eurotom-CEA Association, Fontenay-aux-Roses, Report No. EUR-CEA-FC-761, 1975 (unpublished).
[16]E. S. Marmar, J. E. Rice, J. L. Terry, and F. H. Seguin, Nucl. Fusion **22**, 1567 (1982).
[17]F. Seguin, R. Petrasso, and E. Marmar, Phys. Rev. Lett. **51**, 455 (1983).
[18]N. H. Magee, J. B. Mann, A. L. Merts, and W. D. Robb, Los Alamos National Laboratory Report No. LA-6691-MS, 1977 (unpublished).
[19]P. L. Dufton, K. A. Berrington, P. G. Burke, and A. E. Kingston, Astron. Astrophys. **62**, 111 (1978).
[20]M. Malinovsky, Astron. Astrophys. **43**, 101 (1975).
[21]K. L. Baluja, P. G. Burke, and A. E. Kingston, J. Phys. B **14**, 1333 (1981).
[22]H. Nussbaumer and P. J. Storey, Astron. Astrophys. **64**, 139 (1978).
[23]I. I. Sobelman, L. A. Vainshtein, and E. A. Yukov, *Excitation of Atoms and Broadening of Spectral Lines* (Springer, Berlin, 1981).
[24]W. L. Wiese, M. W. Smith, and B. M. Glennon, *Atomic Transition Probabilities,* Natl. Bur. Stand. Ref. Data Ser., Natl. Bur. Stand. (U.S.) Monograph No. 4 (U.S. GPO, Washington, D.C., 1966).
[25]J. Reader, C. H. Corliss, W. L. Wiese, and G. A. Margin, *Wavelengths and Transition Probabilities for Atoms and Atomic Ions,* Natl. Bur. Stand. Ref. Data Ser., Natl. Bur. Stand. (U.S.) Monograph No. 68 (U.S. GPO, Washington, D.C., 1980).
[26]R. D. Cowan, *The Theory of Atomic Structure and Spectra* (University of California, Berkeley, 1981).
[27]M. J. Seaton, Planet. Space Sci. **12**, 55 (1964).
[28]E. S. Marmar *et al.*, J. Nucl. Mater. **121**, 69 (1984).
[29]A. Hayzen, D. Overskei, and J. Moreno, MIT Plasma Fusion Center Report No. PFC/JA-81-10, 1981 (unpublished).
[30]M. E. Foord, E. S. Marmar, and J. L. Terry, Rev. Sci. Instrum. **53**, 1407 (1982).
[31]S. L. Allen, H. W. Moos, R. K. Richards, J. L. Terry, and E. S. Marmar, Nucl. Fusion **21**, 251 (1981).
[32]J. L. Terry, E. S. Marmar, K. I. Chen, and H. W. Moos, Phys. Rev. Lett. **39**, 1615 (1977).
[33]K. Brau, M. Bitter, R. J. Goldston, D. Manos, K. McGuire, and S. Suckewer, Nucl. Fusion **23**, 1643 (1983).
[34]E. I. Dobrokhatov *et al.*, in *Plasma Physics and Controlled Nuclear Fusion Research,* Proceedings of the 9th International Conference on Plasma Physics and Controlled Nuclear Fusion Research, Baltimore, 1982 (IAEA, Trieste, 1983), Vol. III, p. 229.
[35]J. E. Rice, E. S. Marmar, B. Lipschultz, and J. L. Terry, Nucl. Fusion **24**, 329 (1984).